Manuscript Click here to view linked References

Title: Excitation function of $^{54}Fe(p,\alpha)^{51}Mn$ from 9.5MeV to 18MeV

Authors: *Wilson Lin[1], John T. Wilkinson[2], Kendall E. Barrett[1], Todd E. Barnhart[1], Matthew Gott[3], Kaelyn V. Becker[1], Adam M. Clark[2], Anthony Miller[2], Gunnar Brown[2], Molly DeLuca[2], Robert Bartsch[2], Graham F. Peaslee[2], Jonathan W. Engle[1]

Abstract

Excitation function of the $^{54}Fe(p,\alpha)^{51}Mn$ reaction was measured from 9.5 to 18MeV $E_{0,p+}$ by activating a foil stack of ^{54}Fe electrodeposited on copper substrates. Residual radionuclides were quantified by HPGe gamma ray spectrometry. Both ^{51}Mn ($t_{1/2}$=46.2min, $<E_{\beta+}>$=963.7keV, $I_{\beta+}$=97%; E_γ=749.1keV, I_γ=0.265%) and its radioactive daughter, ^{51}Cr ($t_{1/2}$=27.704d, E_γ=320.1keV, I_γ=9.91%), were used to indirectly quantify formation of ^{51}Mn. Results agree within uncertainty to the only other measurement in literature and predictions of default TALYS theoretical code. Final relative uncertainties are within ±12%.

Keywords: excitation function, gamma spectroscopy, gamma spectrometry, Tandem Van de Graaff accelerator, Mn-51, positron emission tomography

Colored Figures: no figures need coloring

Figure Captions:

Figure 1 A) Example sample target mounted on the aluminum frame for irradiation. The iron thickness was 9.5±0.8μm. B) Target after irradiation. C) Activation profile of the same target, the circular outline depicts a 9mm diameter circle. The intensity is linearly correlated with activity at these levels.

Figure 2. A) Efficiency calibration of the HPGe at UWM with a ^{152}Eu check source approximately 2cm away from the face of the detector. The solid line corresponds to the fit presented in equation 1. B) Residuals of the data to the fit. Horizontal delineations at ±5% and 0% are for visual aid.

Figure 3. Sample spectra acquired from HPGe (+ marker) and the fit applied (solid line) for a target receiving $E_{0,p+}$=18MeV. A) 749keV ^{51}Mn peak acquired at ND, the spectrum was taken 4h post EOB (end of bombardment) with a live time of 600s. Only every second data point is plotted. B) 320keV ^{51}Cr peak acquired at UWM, the spectrum was taken 21d post EOB with a live time of 9000s.

Figure 4. Comparison of the cross section values for $^{nat}Cu(p,x)^{65}Zn$ from this work to IAEA's recommended cross section values[1].

[1]Department of Medical Physics, University of Wisconsin, 1111 Highland Ave., Madison, WI, 53705, United States
[2]Deptartment of Physics, University of Notre Dame, Notre Dame, IN, 46556, United States
[3]Physics Division, Argonne National Laboratory, 9700 South Cass Avenue, Lemont, IL, 60439, United States

Figure 5. Excitation function of $^{54}Fe(p,\alpha)^{51}Mn$ from this work compared with Levkovski's data [2]*. Calculated values from TENDL-2019 is also presented to show the predicted general trend.*

Figure 6. A) Thick target yield at the optimal irradiation time of 83.9minutes using the excitation function measured from this work. The stopping power of protons in iron was taken from SRIM[3]*. B) Comparing the results from this work to that of various ^{51}Mn productions at UWM, including results reported by* [4]*.*

1 Introduction

^{51}Mn ($t_{1/2}$=46.2min, $<E_{\beta+}>$=963.7keV, $I_{\beta+}$=97%; E_{γ}=749.1keV, I_{γ}=0.265%) is a short-lived radionuclide currently being investigated as a potential positron emission tomography (PET) tracer for pancreatic imaging (see [4,5] and references therein). ^{51}Mn has been made by small cyclotrons via $^{50}Cr(d,n)^{51}Mn$ [4], but established techniques for ^{54}Fe target recycling make $^{54}Fe(p,\alpha)^{51}Mn$ more attractive. Only a single measurement of the $^{54}Fe(p,\alpha)^{51}Mn$ excitation function has been reported [2], whereas two measurements of $^{50}Cr(d,n)^{51}Mn$ have been reported [6,7].

We measured the $^{54}Fe(p,\alpha)^{51}Mn$ excitation function on the 11MV FN Tandem Van de Graaff accelerator at University of Notre Dame's (ND) Nuclear Science Laboratory (NSL) with proton energies ($E_{0,p+}$) up to 18MeV and collimated beam widths less than 5mm. Although $E_{0,p+}$=18MeV is below the predicted maximum of the $^{54}Fe(p,\alpha)^{51}Mn$ cross section, it is representative of many commercial cyclotrons [8]. We quantified residuals with ND's on-site high purity germanium detector (HPGe), and corroborated ND spectra with HPGe measurements at University of Wisconsin-Madison (UWM).

We present an experimentally determined excitation function of $^{54}Fe(p,\alpha)^{51}Mn$ from 9.5MeV to 18MeV and discuss clinical relevance based on our results. The measured cross sections include uncertainties in absolute detector efficiency, beam current, counting statistics, number of ^{54}Fe atoms and FN tandem characteristics.

2 Materials and methods

2.1 ^{54}Fe Target Fabrication and Irradiation

Aqueous solutions were made from >18MΩ/cm H_2O. Targets were prepared by electrolytic deposition of isotopically enriched ^{54}Fe metal (99.7% ^{54}Fe, 0.28% ^{56}Fe, 0.01% ^{57}Fe, 0.01% ^{58}Fe; ISOFLEX) on natural copper substrates (99.8% purity, nominally 10μm from Alfa Aesar), in a similar process previously described in [9]. Due to time constraints at ND, and to provide an alternative measure of beam parameters, copper was selected as the backing material to allow simultaneous determination of beam energy and current when assaying ^{51}Mn and ^{51}Cr using $^{nat}Cu(p,x)^{6x}Zn$ monitor reactions. Copper substrates were cut into squares of approximately 1.5x1.5cm^2 and weighed on a calibrated digital scale with sub-milligram precision. The relative uncertainty in the areal density of ^{nat}Cu foils was less than 4%. 50-70mg of ^{54}Fe metallic powder was dissolved in 1mL 6M HCl (concentrated HCl from Fisher Chemical) and 100μl of 30% H_2O_2 (Fisher Chemical). Upon complete dissolution, 10mL of saturated $(NH_4)_2C_2O_4$ Alfa Aesar) was added. The electrolyte was then buffered to pH=4 using 28% NH_4OH (Sigma-Aldrich) and/or 6M HCl and transferred to a cylindrical

plating cell. A platinized titanium mesh anode was positioned approximately 2cm above the copper substrate and a potential of 3.0±0.2V was applied, corresponding to an initial current of 19±3mA. The electroplated region had a diameter of 9.0±0.2mm (average area 0.64cm^2, figure 1A) and electrodeposition lasted 1-2h. Targets were rinsed with ethanol, dried, and weighed (N=3) to determine the plated ^{54}Fe mass, where all measurements were repeatable within ±0.3mg.

Targets were irradiated with $E_{0,p+}$= 9.5MeV-18MeV, where an analyzing magnet filtered incident beam energies to within ±30keV of the setpoint. The analyzing magnet was tuned with deuteron magnetic resonance using a sample of [^{2}H]H_2O. The generating voltmeter along with slit control feedback using the beam helped to monitor the voltage setpoint. Calculated beam energies from ^{6x}Zn products agreed within uncertainty to expected setpoint energies. A titanium hydride cathode served as the source of protons from the Source of Negative Ions by Cesium Sputtering (SNICS) ion source. Beam current was measured on an electrically isolated station connected to the target holder and the beam dump. An external magnetic field was applied to this irradiation line to geometrically suppress leakage of recoil electrons. More information regarding the accelerator can be found in [10–12], where a schematic of the beam setup is provided.

A small correction based on SRIM calculations was applied to the beam energy incident on the copper foils due to interactions with ^{54}Fe (total average energy loss of 140-240keV per ^{54}Fe target). Energies reported for each target were calculated at the midpoint of the material. After irradiation with beam currents of 145-300nA, ranging from fifteen minutes to an hour, the plated ^{54}Fe targets showed no changes in appearance and were well-adhered to the copper backing (see figure 1B). Following irradiation, the targets were left on the sample holder for approximately one hour to reduce exposure to personnel. Then, the samples were transported to the low-background counting station within the NSL with a Canberra model GC3518 high-purity germanium detector (HPGe) and a sample storage area for assaying. The HPGe was surrounded by lead shielding, with the longitudinal axis free for sample placement. After preliminary data were acquired at ND, samples were shipped to UWM for further assay on a different detector (Canberra C1519 HPGe). The detector setup at UWM had no lead shielding above and below the detector but was otherwise shielded by lead.

2.2 Quantification of Activity and Cross Section Evaluation

Radioactivities were quantified by gamma spectrometry using an Al-windowed HPGe and MAESTRO software (ORTEC). ^{152}Eu check sources were used to calibrate the energy and determine the efficiency of the HPGe at ND and UWM. The following function [13]:

$$\ln\left(\eta(E)\right) = A + B\ln(E) + C\ln(E)^2 + D\ln(E)^3 \qquad \text{(Eq. 1)}$$

Was used to fit the efficiency values for gamma emission energies above 240keV (see fig 2). The fit was within ±3% of the data and we observed no improvement in the fit beyond third order in ln(E). Error bars in figure 2 correspond to one standard deviation from counting statistics only. All samples assayed at UWM were placed in the same position, approximately 2cm away from the face of the detector. Samples at ND were placed at various positions to optimize ^{51}Mn signal-to-noise ratio. The impact of coincidence summing was found to be negligible (see figure S2). The activity of the ^{152}Eu check source at UWM was ascertained with a ^{133}Ba check source using the 296keV and 303keV emission from ^{152}Eu and ^{133}Ba, respectively. All check-sources used are traceable to NIST. Gamma

emission intensities and half-lives were all taken from IAEA's nuclear database [14]. HPGe data were cross-referenced between ND and UWM and found to be agreeable within uncertainties. Produced radionuclides relevant to this work are presented in table 1, the chosen gamma emission of interest was used to tabulate peak area and define the region of interest (ROI).

Table 1. Nuclear data of produced radionuclides relevant to this work. Threshold energies were taken from [15]. Radionuclides are not listed if the threshold energy is greater than 18MeV. $^{50}V(p,\gamma)^{51}Cr$ is not listed due to its low significance relative to $^{51}V(p,n)^{51}Cr$.

Radionuclide of interest	Half-life	Gamma emission of interest (keV)	Branching ratio (%)	Production pathway; Threshold energy
^{51}Cr	27.704d	320.08	9.91	$^{51}V(p,n)^{51}Cr$; 1.565MeV Decay of ^{51}Mn
^{51}Mn	46.2min	749.07	0.265	$^{54}Fe(p,\alpha)^{51}Mn$; 3.205MeV $^{52}Cr(p,2n)^{51}Mn$; 16.340MeV
^{56}Co	77.236d	846.77	99.9399	$^{56}Fe(p,n)^{56}Co$; 5.445MeV $^{57}Fe(p,n)^{56}Co$; 13.225MeV
^{62}Zn	9.193h	596.56	26.0	$^{63}Cu(p,2n)^{62}Zn$; 13.477MeV
^{63}Zn	38.47min	669.62	8.2	$^{63}Cu(p,n)^{63}Zn$; 4.215MeV
^{65}Zn	243.93d	1115.54	50.04	$^{65}Cu(p,n)^{65}Zn$; 2.167MeV

A Gaussian and cubic polynomial were used to fit the peak ROI using a non-linear least squares optimization to better estimate the background counts within the ROI:

$$Fit = Ne^{\frac{(x-\mu)^2}{2\sigma^2}} + Ax^3 + Bx^2 + Cx + D \quad \text{(Eq. 2)}$$

The number of bins in the ROI was determined by using four standard deviations of the fitted Gaussian and the total background count was determined as the trapezoidal area from the edges of the fitted ROI. The signal of interest was calculated by subtracting the trapezoidal area from the total raw counts in the ROI. Figure 3. Shows sample spectra taken from the HPGe with their respective fits.

As can be seen from the low signal-to-noise ratio of ^{51}Mn (figure 3A), an appealing alternative for assaying ^{51}Mn is through its longer-lived ^{51}Cr decay product (figure 3B). Although an accurate measure of ^{51}Mn from ^{51}Cr requires a waiting period longer than ten half-lives of ^{51}Mn (>8h), it allows decay of short-lived radionuclides to reduce background in the ROI. Other advantages from assaying ^{51}Cr include the ability to transport samples over long transit times, a more precise half-life, better branching ratio and increased detection efficiency. The "critical level" [16] was chosen as the minimum ^{51}Cr needed to qualitatively distinguish signal from background and set as $1.65\sigma_{background}$ in the energy region of the 320keV peak of interest. This value corresponds to less than 3% of the activity from the

^{54}Fe target with the smallest amount of ^{51}Cr. Background from the bare copper backing was investigated and no detectable ^{51}Cr was observed. Since the bare copper foil did not produce any measurable ^{51}Cr, and that we waited for more than ten half-lives of ^{51}Mn before assaying ^{51}Cr, the ^{51}Cr signal was assumed to be due to the complete the decay of ^{51}Mn. The "cross section" of ^{51}Cr, as obtained from assaying ^{51}Cr, was thus used as an indirect measurement of ^{51}Mn.

A radio- and UV-sensitive phosphor screen was exposed to the activated foils to enable visual inspection of the beam profile. A low intensity UV light was shone perpendicularly above the aluminum-mounted targets to develop a registered profile of the rectangular target frame. The exposed screen was readout with PerkinElmer's Cyclone Plus instrument and digitally processed with OptiQuant software. Contour images of the radiosignal were drawn using MATLAB®. Experiments with point sources (physical radius<1mm) revealed that the true physical distribution was entirely contained within the upper 75% of the max radiosignal. A 20-30% threshold of the max radiosignal was enough to contain >99% of the developed radiosignal within a 9mm diameter circle. A measured activation profile is shown in figure 1C.

Cross sections for the measurements described above were calculated from the activation equation for thin foils (Eq. 3). Given the activity at EOB (end of bombardment), and assuming the irradiation does not produce a parent of the desired radionuclide, the cross section is:

$$\sigma(E) = \frac{A(T_{EOB})}{\lambda l_A \left(e^{-\lambda t'} * I(E,t')\right)|_{T_{EOB}}} \qquad \text{(Eq. 3)}$$

Where * refers to the convolution operator and the bracketed term is evaluated at T_{EOB}, λ is the decay constant of the radionuclide, l_A is the atomic areal density of the target (after correcting for isotopic abundance), $I(E,t)$ is the beam current at a particular energy and T_{EOB} is the irradiation time. Less than 1% difference was observed between convolving the exponential decay of ^{51}Mn with the current signal measured from the chamber and using the average current for all the targets of interest.

The activity at EOB was calculated from the counts registered on the HPGe gamma detector in the following way:

$$A(T_{EOB}) = \frac{N(E)}{t_{live}} \frac{t_{real}}{t_{live}} \frac{\lambda t_{real}}{\eta(E) BR \left(1 - e^{\lambda t_{real}}\right) e^{-\lambda T_{elapsed}}} \qquad \text{(Eq. 4)}$$

Where $N(E)$ is the background subtracted number of counts at a particular ROI, t_{real} is the real time during counting, t_{live} is the live time during counting, $\eta(E)$ is the calibration efficiency for the HPGe detector at a particular energy, BR is the branching ratio of the gamma emission, $T_{elapsed}$ is the time elapsed since EOB at the start of counting.

2.3 Iron Abundance Validation

Though ^{55}Co could theoretically be used to analyze ^{56}Fe impurities, production of ^{55}Co from ^{54}Fe(p,γ)^{55}Co is comparable to ^{56}Fe(p,2n)^{55}Co with a vendor-stated value of 0.3% ^{56}Fe

impurity. At the energies investigated in this paper, the production of ^{56}Co is only possible from ^{56}Fe and ^{57}Fe. With ^{57}Fe(p,2n)^{56}Co cross sections being comparable to ^{56}Fe(p,n)^{56}Co at $E_{0,p+}$=13-18MeV [2], we have assumed the main production pathway of ^{56}Co to be ^{56}Fe(p,n)^{56}Co due to the low vendor-reported ^{57}Fe impurity in our sample (0.01% ^{57}Fe as compared with 0.3% ^{56}Fe). The presence of ^{56}Co was used to determine potential ^{56}Fe impurities by comparing the reported cross section values on EXFOR/literature to those obtained from this work. Explicitly, the relative impurity as an atomic fraction is calculated by:

$$Impurity\ ratio\ = \frac{\sigma_{this\ work}}{\sigma_{literature}} \qquad \text{(Eq. 5)}$$

Where $\sigma_{\text{this work}}$ refers to the cross section of ^{56}Co found from this work, assuming that the entire sample was made of ^{56}Fe, and $\sigma_{\text{literature}}$ is the reported ^{56}Fe(p,n)^{56}Co cross section. ^{nat}Fe(p,x)^{56}Co data from [17] and [18] were used as $\sigma_{\text{literature}}$ after correcting for the 91.75% ^{56}Fe abundance. The determined ^{56}Fe impurity ranged from 0.30-0.47% (see figure S1A), which is in good agreement to isotopic impurity values in the manufacturer-reported ^{54}Fe COA (certificate of analysis). As such, 99.7% ^{54}Fe was used to correct the plated iron mass.

Once all the data were acquired, samples were dissolved in 1.8mL 6M HCl and 0.2mL 30% H_2O_2 and an aliquot of 50µL from the homogenous sample solution was added to 9.950mL of 0.1M HCl. The diluted samples were then analyzed on a Microwave-Plasma Atomic Emission Spectroscopy instrument (4210MP-AES, Agilent Technologies) to quantify iron in the target. Sets of four standard concentrations ranging from 5ppm-100ppm of copper and iron were used for linear calibration curves (R^2>0.999). The mass ratio of copper to iron for each sample was compared between measurements from the scale and MP-AES to eliminate systemic errors from MP-AES. Given that the relative uncertainty of copper's mass from the scale is <2%, the absolute mass of iron was taken to be the mass of copper from the scale multiplied by the mass ratio of copper to iron as obtained from MP-AES. Copper was analyzed using wavelengths of 324.754nm, 327.395nm and 510.554nm, and iron was analyzed using wavelengths of 371.993nm and 438.354nm. The selected wavelengths were chosen to maximize the intensity, provide redundancy and to avoid overlap with other elements from MP-AES. The system was operated at a constant, stable temperature throughout each independent measurement (N=3, each performed in triplicate). The final mass of ^{54}Fe used in computing the cross section was taken to be the weighted (reciprocal variance) average of measurements from the scale and the MP-AES. All mass measurements from the scale agreed within uncertainty to that of MP-AES except for target 5, where the average mass differed by +7% (.3mg) from that of the scale (see figure S1B). The dissolved iron was then separated from copper (via precipitation of copper oxalate) and recycled for ^{54}Fe target fabrication.

2.4 Uncertainties

Uncertainties in this work correspond to one standard deviation about the mean reported value. The Poisson heuristic was applied to determine the uncertainty from registered counts on the HPGe. Uncertainties of 6% and 5% were assumed for the HPGe efficiency calibration and the current registered from the electrically isolated chamber, respectively. The efficiency calibration uncertainty accounts for the uncertainty in the ^{152}Eu activity (4%), the fit (3%) and slight differences between target geometry and position from the HPGe

(3%). Due to the relatively low power transfer to the targets, recoil losses were considered negligible from the current reading. Since the desired $E_{0,p+}$ was well within 100keV of the setpoint, energy uncertainties are simply reported as ±0.1MeV to include stopping power effects throughout the ^{54}Fe layer. Uncertainties from MP-AES were evaluated experimentally by having N=3 repeated measurements of known standard concentrations and samples (each performed in triplicate); uncertainties, including calibration, were within 8%. The ^{51}Cr activity, as calculated from the HPGe spectra at ND and UWM after decay correcting to EOB, were combined into a weighted average (reciprocal variance of activity at EOB) to reduce uncertainties from HPGe quantification. The final absolute uncertainty is the result of summing the appropriate relative errors in quadrature and scaling with the cross section.

3 Results and Discussion

3.1 IAEA ^{nat}Cu(p,x)^{65}Zn Monitor Reaction

The measured ^{65}Zn cross section agrees within uncertainty to IAEA's recommended values [1] (see figure 4). The 1115keV gamma emission of ^{65}Zn was used to tabulate the peak area.

3.2 ^{54}Fe(p,α)^{51}Mn excitation function

The resulting excitation function is plotted in figure 5 against calculated values from TENDL-2019 and experimental data from Levkovski [2]. Explicit values of cross section from this work can be found in table 2. Although the directly obtained ^{51}Mn cross sections had high uncertainties and deviations from the reported value, they still agree with cross sections calculated from ^{51}Cr quantification. The 749keV gamma emission of ^{51}Mn and 320keV gamma emission of ^{51}Cr were used to tabulate their respective peak areas. Data below the limit of detection (as described earlier) are labelled as 'N/A'. Most of our data agrees with [2] within uncertainties, and especially so if an approximate 10% reduction is applied for reported cross sections above 15MeV. This potential systematic difference is corroborated by reports that [2] may have slightly overestimated values of its monitor reaction [8]. Theoretical predictions from TENDL-2019 were generally lower than Levkovski's experimental results and in better agreement with this work, but the shape of the excitation function is consistent between all sources.

Table 2. Measured ^{54}Fe(p,α)^{51}Mn cross sections from this work using the two techniques described previously, and with an intercomparison between UWM and ND. The presence of ^{51}Cr was only possible due to the decay of ^{51}Mn and not from proton induced reactions in our sample. Cross sections measured using ^{51}Cr are labelled as such. Cross sections computed using a weighted average of ^{51}Cr activity at ND and UWM are also reported.

Midpoint energy ±0.1 [MeV]	σ [mb] *from ^{51}Cr at UWM	σ [mb] *from ^{51}Cr at ND	σ [mb] *from ^{51}Mn at ND	σ [mb] *Weighted average of ^{51}Cr from UWM and ND
17.9	41.5±3.7	41.5±4.7	26.4±12.9	41.5±3.1
16.9	39.6±3.6	43.2±4.8	52.5±18.6	40.5±3.7

15.9	37.7±3.3	40.7±8.4	N/A	37.8±2.9
14.9	33.2±3.1	33.7±3.8	18.5±10.2	33.4±2.5
13.9	31.9±3	35±3.5	N/A	33.1±3.2
12.9	22.7±2.1	23.4±2.5	N/A	22.9±1.8
11.9	15.9±1.5	16.4±2.1	N/A	16.0±1.2
10.9	7.44±0.74	7.88±1.45	N/A	7.49±0.59
9.9	2.29±0.22	2.9±0.56	N/A	2.33±0.28
9.4	0.83±0.09	1.03±0.41	N/A	0.84±0.08

3.3 Optimal ^{51}Mn production parameters

The "optimal" irradiation time:

$$t_{optimal} = argmax_t(\frac{A_{51Mn}}{A_{51Cr}} A_{51Mn}) \quad \text{(Eq. 6)}$$

was found to be approximately 1.4h and results in roughly 72% of the saturated yield. In equation 6, A_{51Mn} is the activity of ^{51}Mn at EOB and A_{51Cr} is the total activity of ^{51}Cr once ^{51}Mn has fully decayed. $t_{optimal}$ can be interpreted as the irradiation time that reduces the relative amount of ^{51}Cr produced while simultaneously maximizing A_{51Mn}. Reducing the irradiation time reduces the total amount of any radionuclides produced but one advantage is that it also reduces the relative amounts of ^{56}Co and ^{55}Co, a potential source of concern in clinical productions of ^{51}Mn. The optimal areal density of the target, with respect to cost, was found to be 181mg/cm^2 at 16.1MeV and corresponds to about 89% of the thick target yield, when all other parameters are considered equal. Increasing the areal density increases the relative amounts of ^{56}Co and ^{55}Co since their relative cross sections are heavily favored at lower energies. Despite this potential concern, separation of manganese from cobalt using an extraction resin functionalized with N,N,N′,N′-tetrakis-2-ethylhexyldiglycolamide (branched DGA, Eichrom™) has been reported [9,19]. Explicitly, to maximize the ^{51}Mn yield, an areal density of 270mg/cm^2 is thick to a 16.1MeV proton beam.

Using the optimal irradiation time and the data obtained from this work, a thick target yield [20] over the energies investigated is presented in figure 6A. A cubic spline interpolation was used to generate finer cross section and stopping power values for integration. A 16.1MeV, 30μA proton beam impinging on a target with areal density of 181mg/cm^2 1.4h will form 7.62GBq of ^{51}Mn at EOB. Yields from ^{51}Mn production at UWM with a PETtrace™ cyclotron (GE Healthcare) are compared to the results of this work (figure 6B), where the irradiation time has been normalized to 1.4h. Production of radionuclides from electrodeposited targets at UWM have used targets that do not fully intercept the beam. A correction factor of about 2 on average (varies for each irradiation) was determined from radiochromic film and analyzing the resulting beam geometry relative to a 1cm diameter target [21]. The calculated yield obtained from this work agrees well to the productions at UWM with this correction factor.

Nevertheless, our results (ideal and practical) show that using ^{54}Fe targets with an areal density of 100mg/cm^2 can yield clinically relevant quantities of ^{51}Mn at EOB (>3.5GBq) with just 40μAh (40μA, 1h) using the PETtrace™. The previous statement assumes that personnel handling ^{51}Mn will achieve an end of chemistry yield >740MBq, which has already been accomplished by [4] if scaled by the EOB yield.

4 Conclusion:

The results presented in this article corroborate within uncertainty the work of Levkovski. Gamma spectrometric assays from UWM were consistent with results from ND, and ^{65}Zn cross section data from this work agrees within uncertainties to IAEA's recommended dataset. Electrodeposition of ^{54}Fe onto ^{nat}Cu foils was instrumental in fabricating thin-foil targets. Thick target yields at the optimal time point and optimal target areal densities were also presented using the data acquired from this work and compared to production of ^{51}Mn at UWM, with results agreeing after correcting for beam-target incidence. To our knowledge, this work is the first investigation of ^{54}Fe(p,α)^{51}Mn excitation function presented in a peer reviewed publication. We hope these results enable optimization of routine ^{51}Mn production using the globally distributed constellation of small cyclotrons and accelerators.

Acknowledgement:

This work would not have been possible without the support from the Institute for Structure and Nuclear Astrophysics group and the associated Nuclear Science Laboratory at the University of Notre Dame. The authors would like to thank Edward Stech of ND for his technical support in operating the accelerator as well as logistics associated with radiation safety. Jonathan W. Engle and Kaelyn V. Becker are grateful for support from the Department of Energy Office of Science Isotope Program (awards DE-SC0020417), and Jonathan W. Engle and Wilson Lin are grateful for support from NIH/NCI award P01-CA250972. Adam M. Clark is grateful for the support from the NSF under grant No. PHY-2011890 as well as the U.S. Nuclear Regulatory Commission award 31310019M0037.

Competing Interests:

The authors declare that they have no competing interests.

References:

[1] Hermanne A, Ignatyuk AV, Capote R, Carlson BV, Engle JW, Kellett MA, et al. Reference Cross Sections for Charged-particle Monitor Reactions. Nuclear Data Sheets 2018;148:338–82. https://doi.org/10.1016/j.nds.2018.02.009.

[2] Levkovski VN. *Cross-Section of medium Mass Nuclide Activation (A=40–100) by Medium Energy Protons and Alpha Particles*. Inter-Vesi, Moscow: 1991.

[3] Ziegler JF, Ziegler MD, Biersack JP. SRIM - The stopping and range of ions in matter (2010). Nuclear Instruments and Methods in Physics Research B 2010;268:1818–23. https://doi.org/10.1016/j.nimb.2010.02.091.

[4] Graves SA, Hernandez R, Valdovinos HF, Ellison PA, Engle JW, Barnhart TE, et al. Preparation and in vivo characterization of 51MnCl2 as PET tracer of Ca2+ channel-mediated transport. Sci Rep 2017;7:3033. https://doi.org/10.1038/s41598-017-03202-0.

[5] Hernandez R, Graves SA, Gregg T, VanDeusen HR, Fenske RJ, Wienkes HN, et al. Radiomanganese PET Detects Changes in Functional β-Cell Mass in Mouse Models of Diabetes. Diabetes 2017;66:2163–74. https://doi.org/10.2337/db16-1285.

[6] Klein ATJ, Rösch F, Qaim SM. Investigation of 50Cr(d,n)51Mn and natCr(p,x)51Mn processes with respect to the production of the positron emitter 51Mn. Radiochimica Acta 2000;88:253–64. https://doi.org/10.1524/ract.2000.88.5.253.

[7] Cogneau M, Gilly L, Cara J. Absolute cross sections and excitation functions for deuteron induced reactions on chromium between 2 and 12 MeV. Nuclear Physics 1966;79:203–8. https://doi.org/10.1016/0029-5582(66)90403-2.
[8] IAEA. Charged particle cross-section database for medical radioisotope production: diagnostic radioisotopes and monitor reactions 2001. https://www-pub.iaea.org/MTCD/Publications/PDF/te_1211_prn.pdf (accessed August 27, 2021).
[9] Valdovinos HF, Hernandez R, Graves S, Ellison PA, Barnhart TE, Theuer CP, et al. Cyclotron production and radiochemical separation of 55Co and 58mCo from 54Fe, 58Ni and 57Fe targets. Applied Radiation and Isotopes 2017;130:90–101. https://doi.org/10.1016/j.apradiso.2017.09.005.
[10] McGuinness SR. A Heavy-Ion Approach to Radiomedicine. University Of Notre Dame, 2021.
[11] McGuinness SR, Wilkinson JT, Peaslee GF. Heavy-ion production of 77Br and 76Br. Sci Rep 2021;11:15749. https://doi.org/10.1038/s41598-021-94922-x.
[12] Skulski M, Anderson T, Callahan L, Clark AM, Nelson AD, Robertson D, et al. Recent developments in the AMS system at the Nuclear Science Laboratory: Impacts on radionuclide sensitivities and current capabilities. Nuclear Instruments and Methods in Physics Research Section B: Beam Interactions with Materials and Atoms 2021;488:30–6. https://doi.org/10.1016/j.nimb.2020.12.009.
[13] Molnár GL, Révay Zs, Belgya T. Wide energy range efficiency calibration method for Ge detectors. Nuclear Instruments and Methods in Physics Research Section A: Accelerators, Spectrometers, Detectors and Associated Equipment 2002;489:140–59. https://doi.org/10.1016/S0168-9002(02)00902-6.
[14] From ENSDF database as of August 28, 2021. Version available at http://www.nndc.bnl.gov/ensarchivals/
[15] Pritychenko B, Sonzogni A. Q-value Calculator (QCalc) n.d. https://www.nndc.bnl.gov/qcalc/ (accessed August 30, 2021).
[16] Currie LA. Limits for qualitative detection and quantitative determination. Application to radiochemistry. Anal Chem 1968;40:586–93. https://doi.org/10.1021/ac60259a007.
[17] Takács S, Vasváry L, Tárkányi F. Remeasurement and compilation of excitation function of proton induced reactions on iron for activation techniques. Nuclear Instruments and Methods in Physics Research Section B: Beam Interactions with Materials and Atoms 1994;89:88–94. https://doi.org/10.1016/0168-583X(94)95152-7.
[18] Al-Abyad M, Comsan MNH, Qaim SM. Excitation functions of proton-induced reactions on natFe and enriched 57Fe with particular reference to the production of 57Co. Applied Radiation and Isotopes 2009;67:122–8. https://doi.org/10.1016/j.apradiso.2008.07.006.
[19] Barrett KE, Aluicio-Sarduy E, Olson AP, Kutyreff CJ, Ellison PA, Barnhart TE, et al. Radiochemical isolation method for the production of 52gMn from natCr for accelerator targets. Applied Radiation and Isotopes 2019;146:99–103. https://doi.org/10.1016/j.apradiso.2019.01.025.
[20] Definitions of radioisotope thick target yields n.d. https://www.degruyter.com/document/doi/10.1515/ract-2013-2234/html (accessed August 28, 2021).

[21] Valdovinos H, Hernandez R, Goel S, Graves S, Barnhart T, Cai W, et al. Cyclotron production of 58mCo for Auger electron-based targeted radioimmunotherapy and PET imaging post-therapy with the daughter 58gCo. J Nucl Med 2016;57:332–332.

Click here to access/download;Figure;FIG1.eps

A)

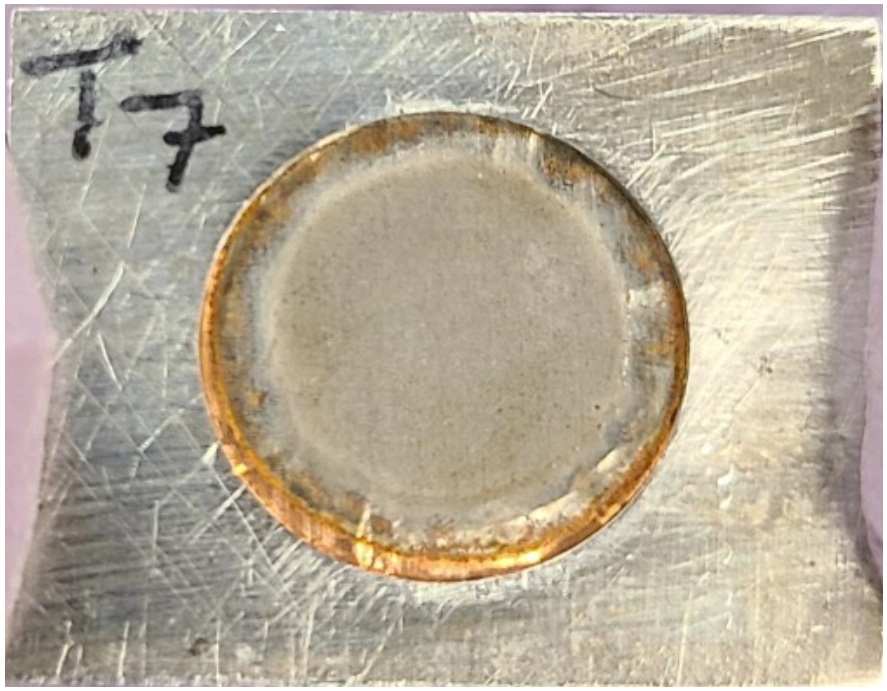

B)

C)

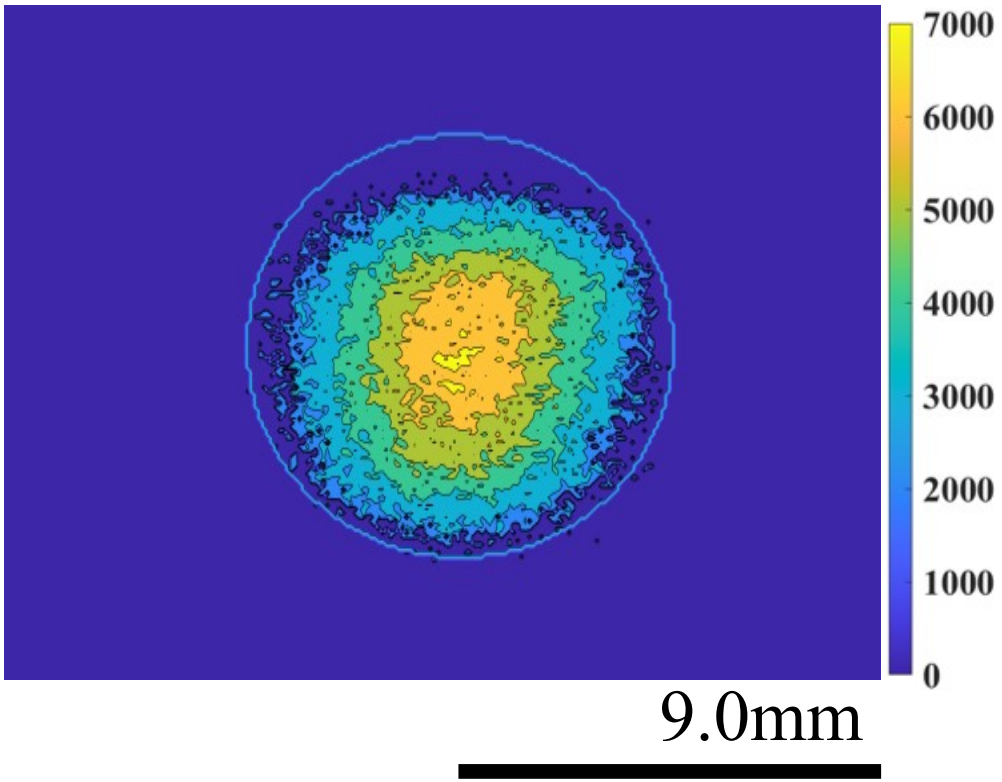

Click here to access/download;Figure;FIG3.eps

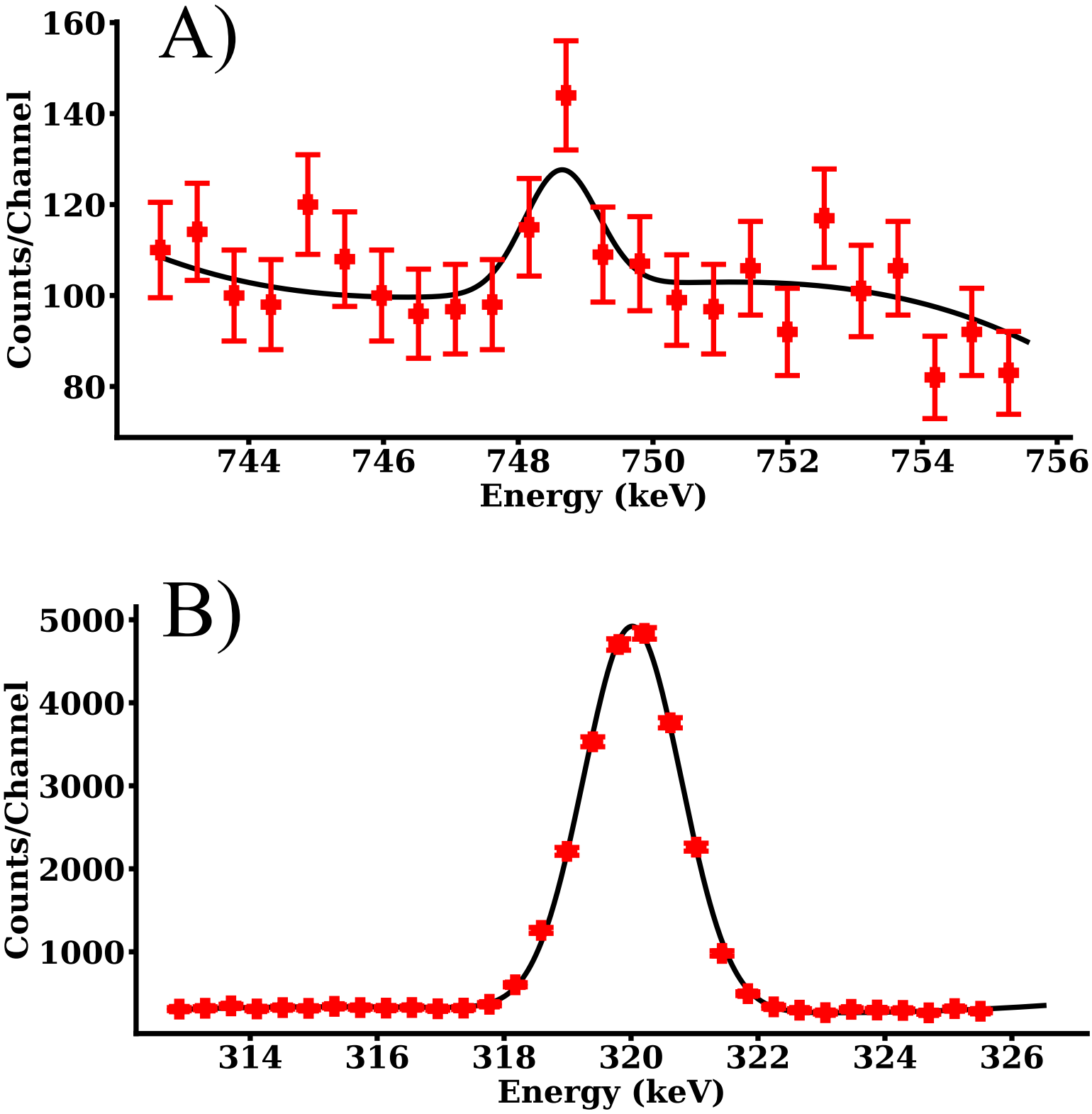

Click here to access/download;Figure;FIG6.eps

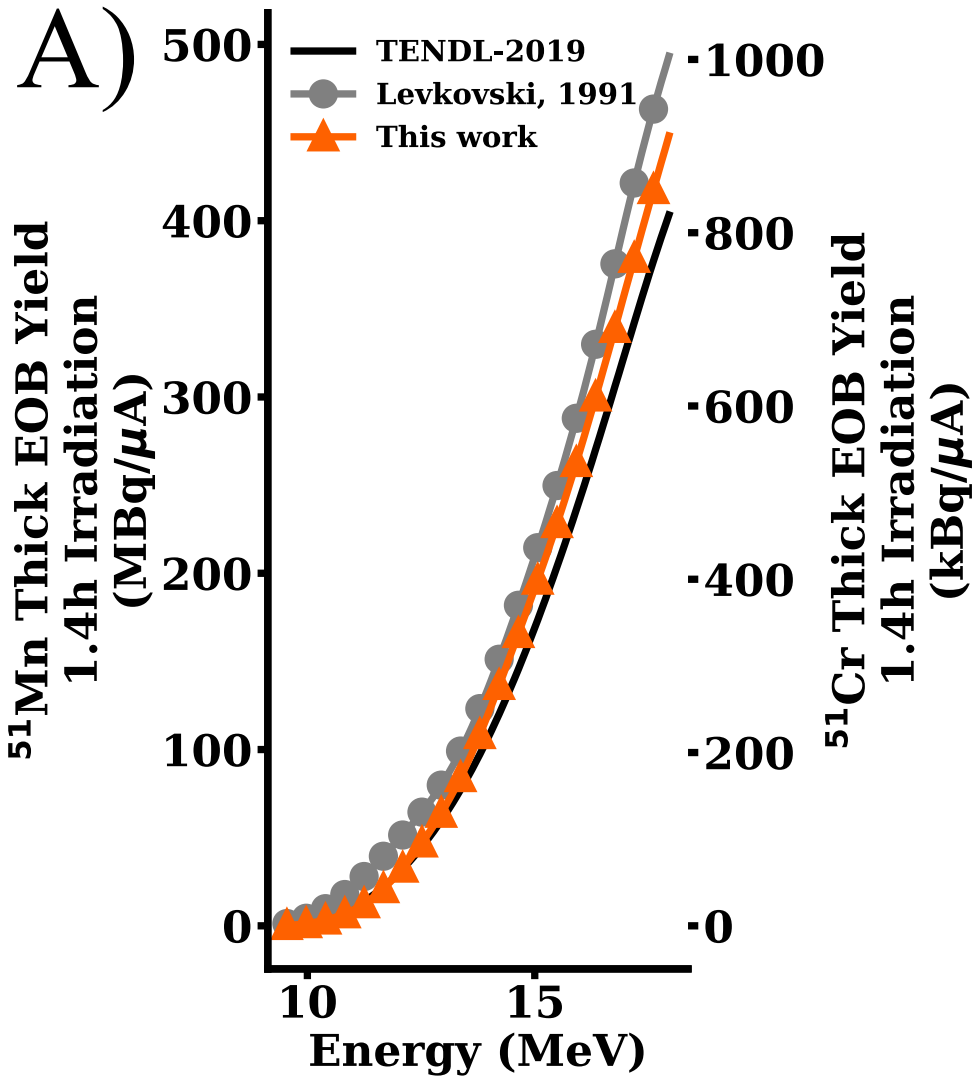

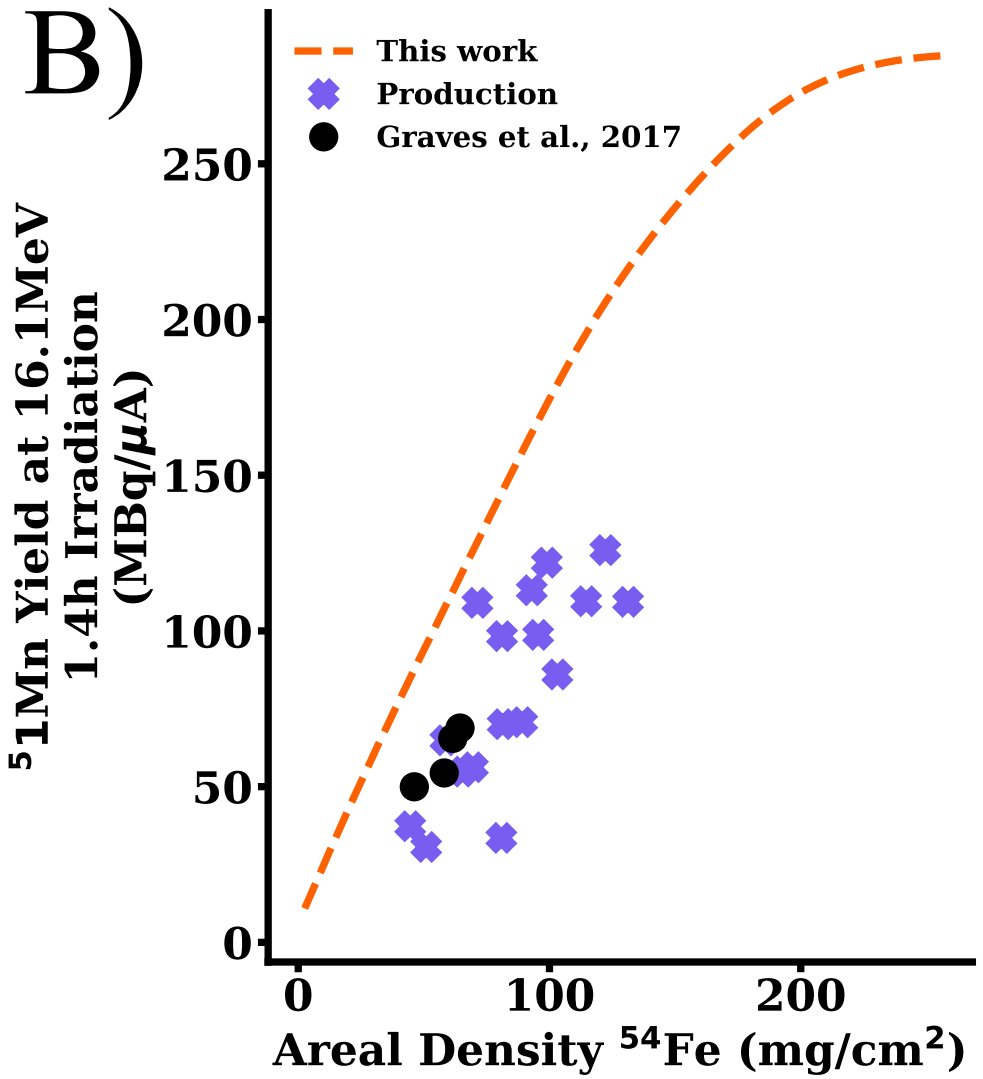

Figure2

Click here to access/download;Figure;FIG2_REV2.eps

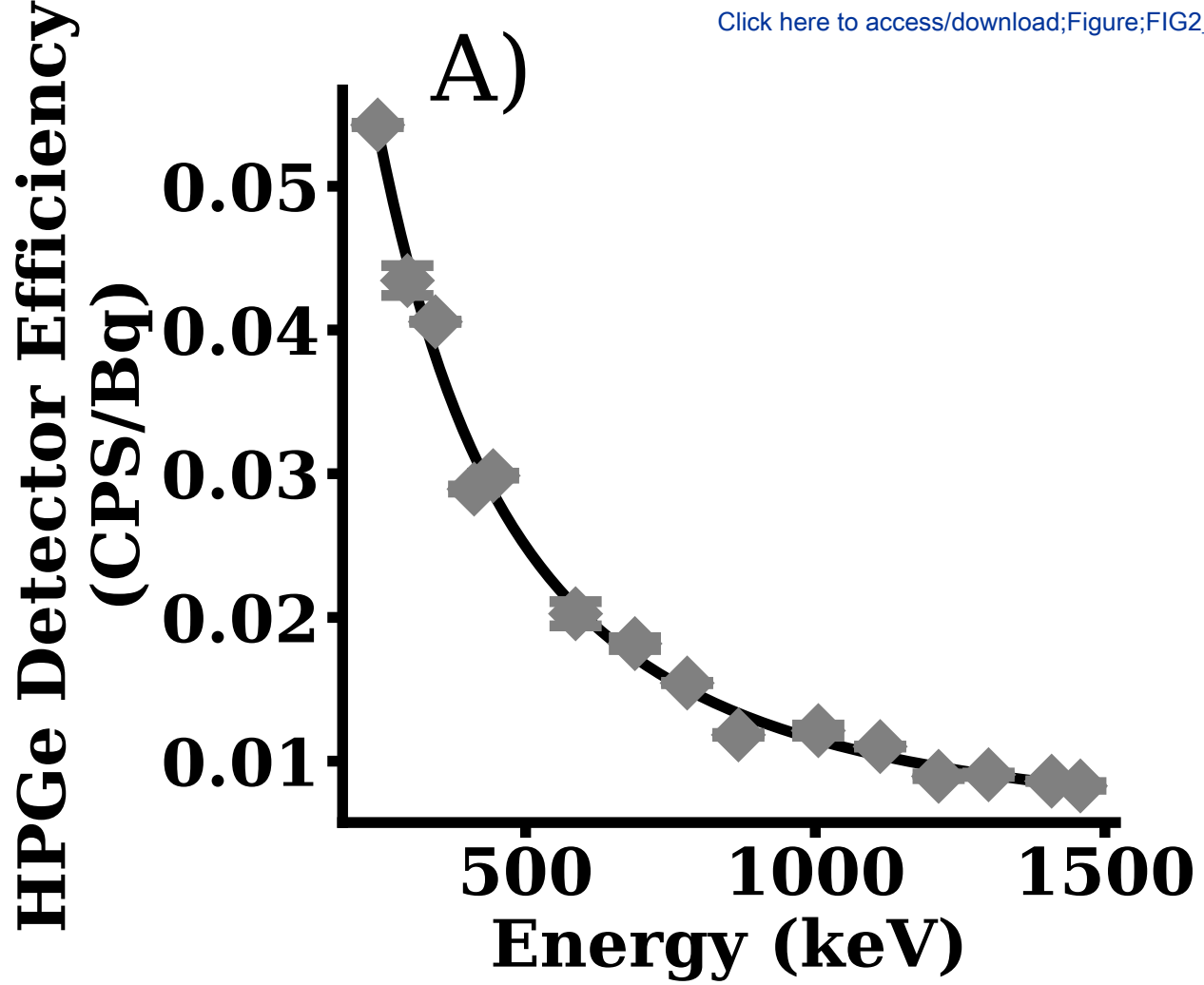

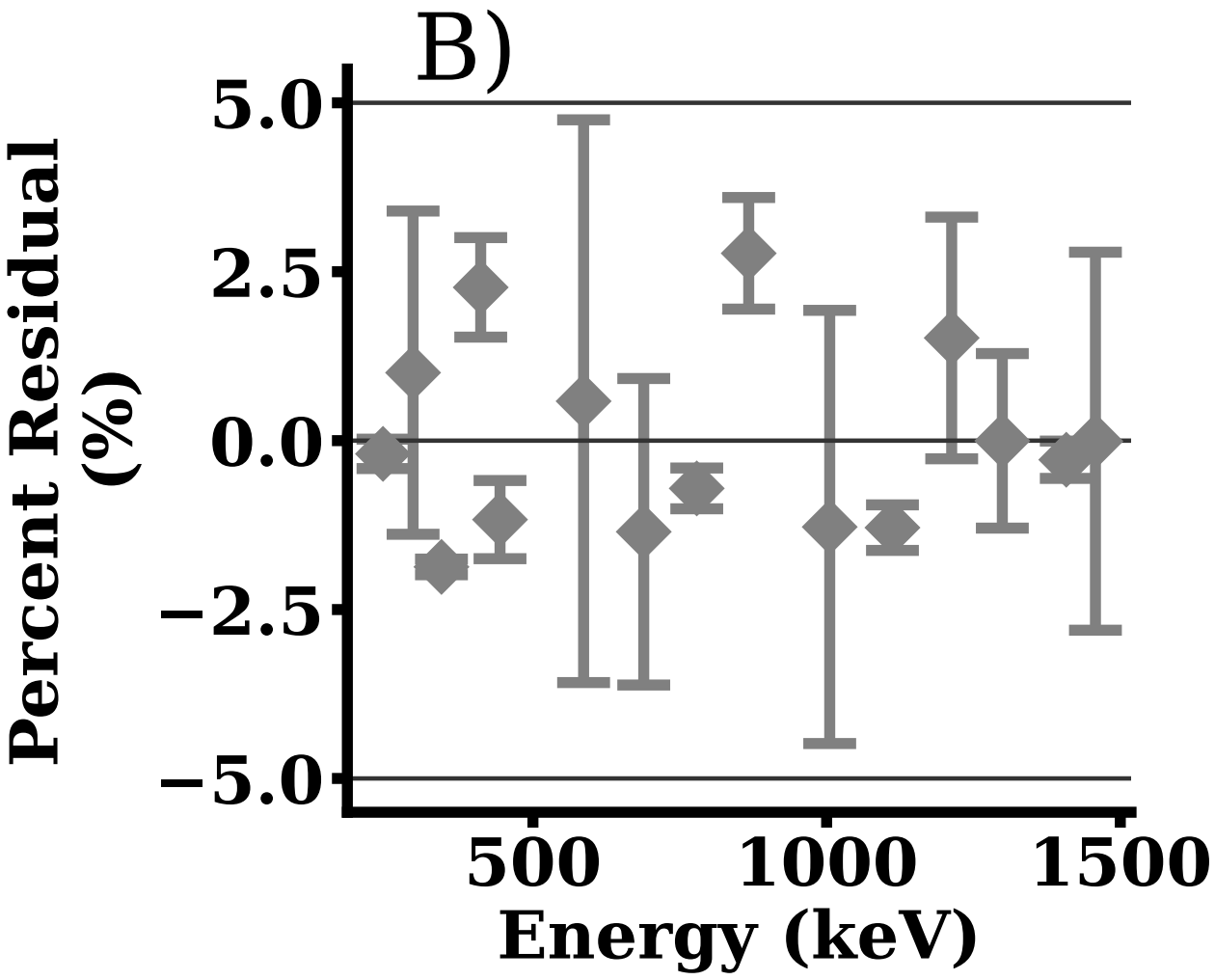

Figure4

Click here to access/download;Figure;FIG4_REV2.eps

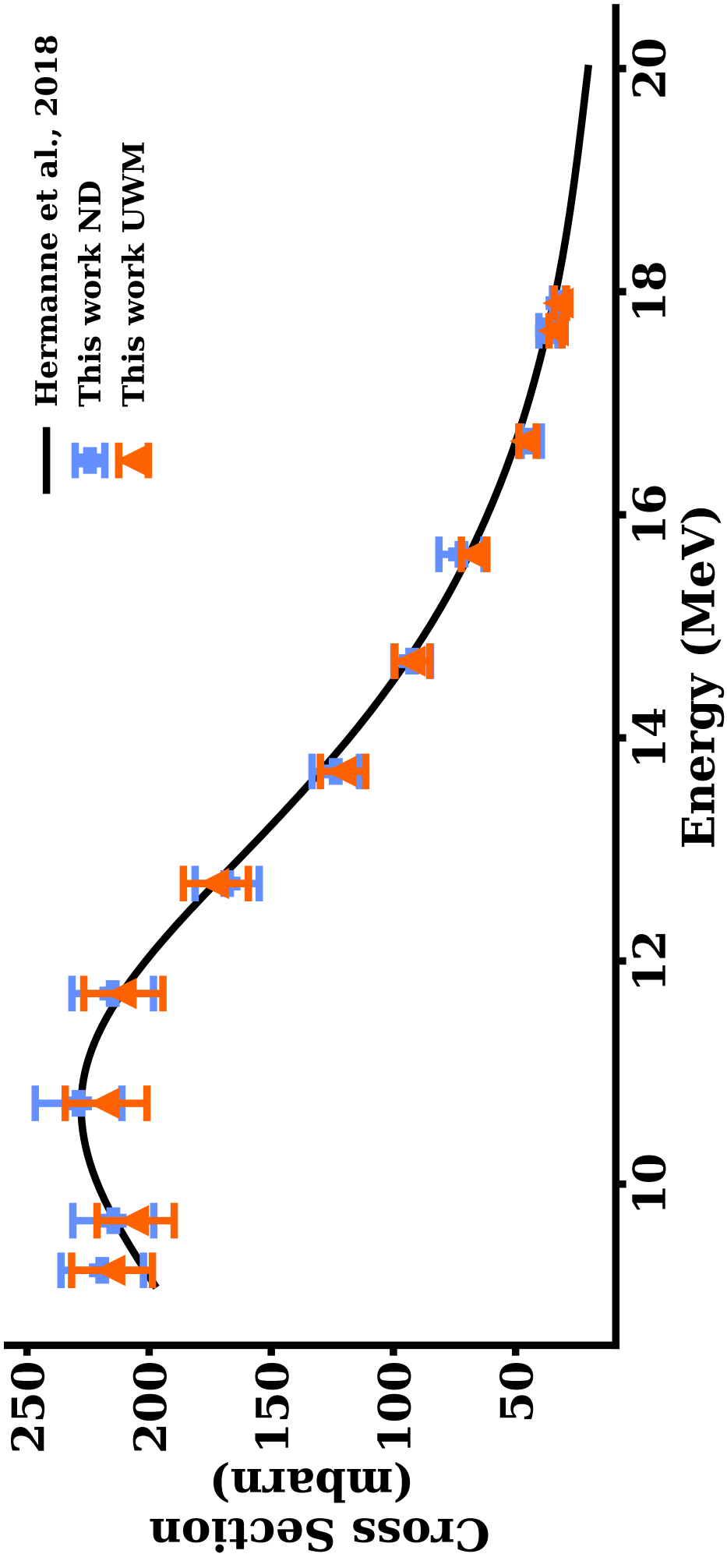

Click here to access/download;Figure;FIG5_REV2.eps

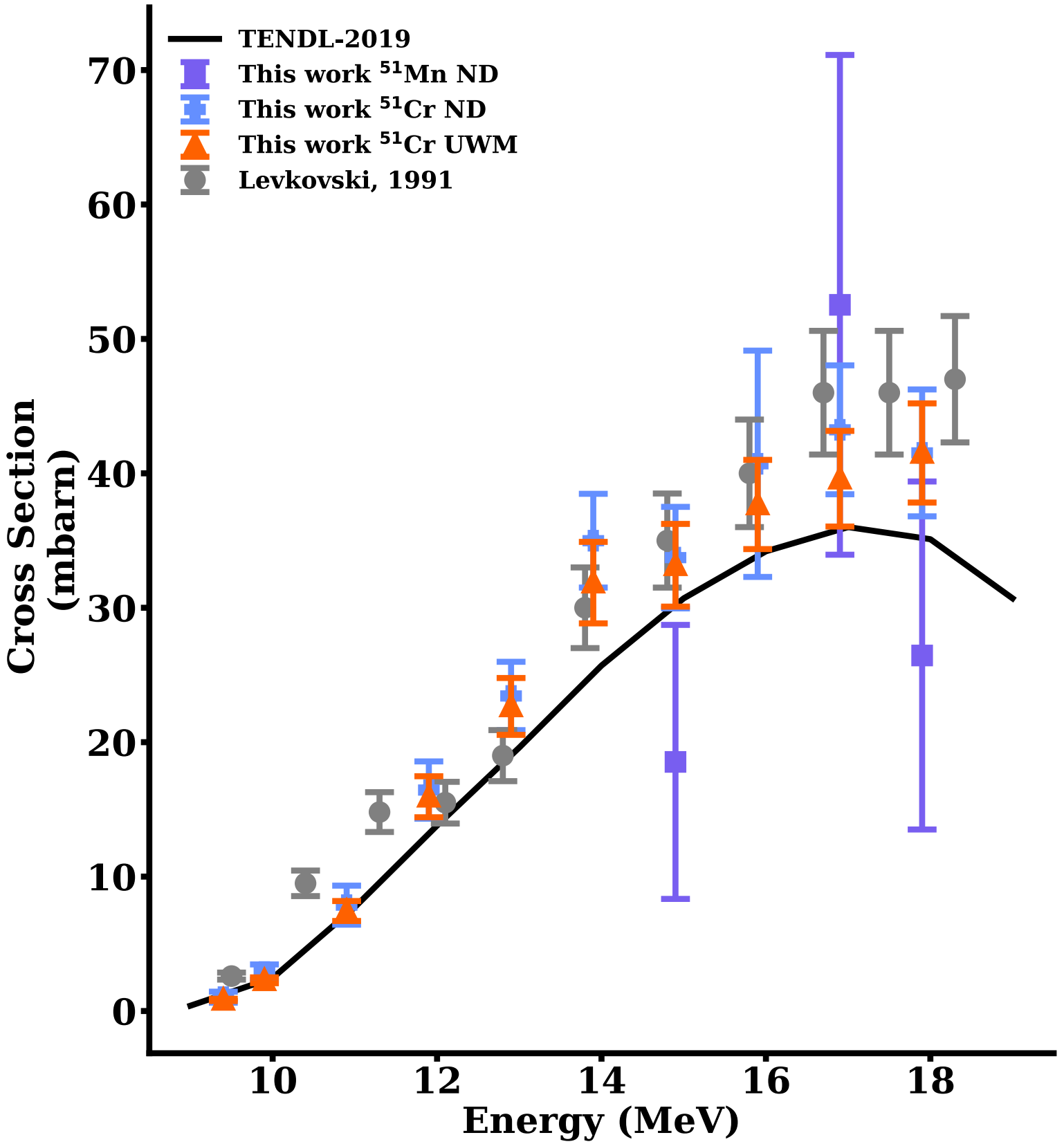

Click here to access/download
Supplementary material for on-line publication only
Supplementary Materials.docx

Declaration of interests

☒ The authors declare that they have no known competing financial interests or personal relationships that could have appeared to influence the work reported in this paper.

☐The authors declare the following financial interests/personal relationships which may be considered as potential competing interests:

Author Contributions:

Wilson Lin: methodology, software, validation, formal analysis, investigation, writing-original draft and review & editing, visualization
John T. Wilkinson: methodology, investigation, writing-review & editing, visualization
Kendall E. Barrett: investigation, writing-review & editing, visualization
Todd E. Barnhart: methodology, resources, writing-review & editing, supervision
Matthew Gott: methodology, investigation, resources, writing-review & editing
Kaelyn V. Becker: software, writing-review & editing
Adam M. Clark: methodology, writing-review & editing
Anthony Miller: investigation, writing-review & editing
Gunnar Brown: writing-review & editing
Molly DeLuca: writing-review & editing
Robert Bartsch: writing-review & editing
Graham F. Peaslee: methodology, resources, writing-review & editing, supervision, project administration, funding acquisition
Jonathan W. Engle: conceptualization, methodology, resources, review & editing, visualization, supervision, project administration, funding acquisition